



Hierarchical-interface design for stable helium storage and structural evolution in homogeneous nano-multilayered $\text{Al}_{1.5}\text{CoCrFeNi}$ high entropy alloy films

Guo Pu^a, Qiran Li^b, Yihan Wang^{a,*}, Jia Li^a, Sheng Chen^a, Kun Zhang^a, Chi Yang^c, Zhijun Wang^c, Liwei Lin^a, Ding Ren^a, Zongbiao Ye^a, Bin Liu^d, Bo Liu^{a,*}

^a Key Laboratory of Radiation Physics and Technology of Ministry of Education, Institute of Nuclear Science and Technology, Sichuan University, Chengdu 610064, PR China

^b Shenzhen Institutes of Advanced Technology, Chinese Academy of Sciences, Shenzhen 518055, PR China

^c Institute for Advanced Study, Chengdu University, Chengdu 610106, PR China

^d Powder Metallurgy Research Institute, Central South University, Changsha 410083, PR China

ARTICLE INFO

Keywords:

Hierarchical-interface
He bubbles
High entropy alloy films
Helium management
Phase transformation

ABSTRACT

Hierarchical interfaces and nanometer grain boundaries (GBs) were synchronously designed inside the homogeneous $\text{Al}_{1.5}\text{CoCrFeNi}$ high entropy alloy (HEA) nano-multilayered films, in which each lamellae was composed of nano-crystals to construct helium (He) ion radiation-tolerant materials used for future advanced nuclear-energy system. The depth profile of He behavior and phase-structure evolution in the irradiated $[\text{Al}_{1.5}\text{CoCrFeNi} (10 \text{ nm})]_{30}$ and $[\text{Al}_{1.5}\text{CoCrFeNi} (30 \text{ nm})]_{10}$ nano-multilayered films were investigated systematically. Results indicated that the He bubble size in multilayered film exhibited a reduction tendency and a wide distribution feature as the individual-thickness increased from 10 nm to 30 nm, demonstrating inverse results with previous heterogeneous-interface modeling. Reduced bubble pressures were identified in the two kinds of nano-multilayered HEA films, indicating that the coexistence of nanocrystals and homogeneous-interfaces was beneficial to manage He distribution and prolonged bubble growth effectively by tailoring each-lamellae size in these two kinds of multilayered $\text{Al}_{1.5}\text{CoCrFeNi}$ HEA films. Partial phase transformation from body-centered-cubic (BCC) to face-centered-cubic (FCC) structure was induced through promoting the structural evolution between the irradiation-induced amorphous regions and compositional reorganization in these nano-multilayered HEA films upon irradiation. The interfaces and GBs promoted the annihilation of these defects and further facilitated the self-healing behavior. Such hierarchical-interface in the HEA provides a novel strategy for the effective He entrapment in improving radiation tolerance and a potential possibility of real-application.

1. Introduction

The newly proposed high entropy alloys (HEAs), composed of multiple principal elements with (nearly) equimolar ratio, have elicited widespread attention on account of their advantageous mechanical properties, corrosion resistance and radiation tolerance compared to the conventional steels and alloys [1–10]. These outstanding properties make HEA one of the most attractive candidate materials for future advanced reactor system. However, after being long-term exposed to the relevant irradiation conditions, numerous helium (He) atoms originated from the byproduct of the (D, T) reaction or (n, α) nuclear transmutation reaction are easy to precipitated into nano-meter gas bubbles because of

its insolubility in these structural-materials [11]. Unlike the He-free cavities, these bubbles can facilitate nucleation for the growth of larger voids and degrade mechanical properties by aggravating radiation-induced He embrittlement [12], volume swelling [13], and surface deterioration [14]. Therefore, exploring novel strategies to design HEAs with further enhanced capability to manage He defect is a pivotal mission to overcome the susceptibility to failure under He⁺ irradiation conditions.

The available approaches to reduce the detrimental effects of irradiation-induced He defect in alloy materials were generally based on tuning the bubble distribution and delaying the “bubble-to-void” transformation during He⁺ irradiation [14]. The critical fluence of

* Corresponding authors.

E-mail addresses: yhwang027@scu.edu.cn (Y. Wang), liubo2009@scu.edu.cn (B. Liu).

<https://doi.org/10.1016/j.surfcoat.2022.128393>

Received 28 February 2022; Accepted 21 March 2022

Available online 29 March 2022

0257-8972/© 2022 Elsevier B.V. All rights reserved.

implanted He in alloys required to transform stable bubbles into voids could be enhanced by decreasing the concentration of radiation-induced vacancies and increasing the nucleation density of bubble [15,16]. The nano-meter oxide/carbide dispersion strengthened (ODS/CDS) alloys have been designed to resist He induced damage based on the entrapment effect of defect sink at the oxide/carbide precipitates [17,18]. These nano-scale precipitates with a dispersed distribution character can further facilitate the recombination rate of irradiation-induced point defects (thereby reducing vacancy or interstitial supersaturation) and disperse the implanted He to numerous disconnected trapping sites at the interfaces between precipitated particles and their alloy matrix, giving rise to a stable storage through numerous small and stable bubbles. On the other hand, one noteworthy pathway proposed in the past decade to restrain the deleterious effects of He atoms and irradiation-induced extended defects in alloys is to apply the high-density grain boundaries (GBs) and hetero-interfaces with hierarchical-structure in materials [19]. In our previous work, high-density GBs in nanocrystalline $\text{Al}_{1.5}\text{CoCrFeNi}$ HEA films were successfully achieved and result showed that the transformation of He clusters into bubbles was suppressed due to the dispersed distribution of He defect along the GB in HEA matrix [20]. Many experimental studies also demonstrated that the heterogeneous phase interfaces, such as those in Cr/W [21], V/Cu [22], and Nb/Cu [23] multi-layered nano-films, can delay the formation of He bubbles in these films due to the stable storage of implanted He at interface. The growth of He bubbles was totally inhibited at high-density interfaces through tailoring the individual-thickness of each layer to several nanometer [22,23]. Meanwhile, multi-scale modeling has verified that the semi-coherent interface contributes to retarding the formation of He bubbles because He atoms are stored in stable nano-scale platelet-shaped clusters at the semi-coherent interface in the heterogeneous dual-phase film layers [24]. Moreover, previous result has revealed that He bubbles at FeCoCrNi/Cu, Nb/Cu interfaces tended to diffuse into Cu film matrix because of its different surface energy and elastic modulus, which seriously prompt high-pressured He bubble migration and growth in the second phase (the Cu phase) [23,25]. Up to now, the storage of He atom in the HEA candidates remains a noteworthy and thorny problem. Based on the understanding of prominent entrapment-ability of He atom at GBs or interphase boundaries, it is urgent to develop effective strategy that the introduced homogeneous-

interfaces can trap He atoms in the multilayered HEA with a single-phase structure. Therefore, it is worthwhile to explore the influence of coexistence effect of nanocrystals and hierarchical-interfaces on the detailed He storage behavior and irradiation-induced structural evolution in the multilayered HEA films with homogeneous composition.

In this work, we prepared $\text{Al}_{1.5}\text{CoCrFeNi}$ HEA multi-layered films composed of nano-crystals to highlight the role of hierarchical-interface in trapping and storing He atoms in a stable way under the He^+ irradiation conditions. As shown in the Fig. 1, the construction of a typical homogeneous-interface was illustrated in the $\text{Al}_{1.5}\text{CoCrFeNi}$ HEA films. The nominal total thickness of the nano-multilayered $\text{Al}_{1.5}\text{CoCrFeNi}$ HEA films is about 300 nm, and individual thickness in film layers is approximately 10 nm and 30 nm, the corresponding total-layers are 30 and 10, respectively, (referred to as $[\text{Al}_{1.5}\text{CoCrFeNi} (10 \text{ nm})]_{30}$ and $[\text{Al}_{1.5}\text{CoCrFeNi} (30 \text{ nm})]_{10}$ in the subsequent paragraphs) to regulate the interface number. During He^+ irradiation, vast interfaces generated enough defect sinks (vacancy and interstitial) for trapping He atoms to delay the bubble growth, these defect sinks were introduced due to the atom-size discrepancy resulted in lattice mismatch. Besides, the introduced nano-GBs in film matrix provide favorable diffusion-channels for the migration of He atoms into interfaces, reducing the probability of trapping He atom by the vacancies inside grains themselves. Based on the experimental results, we found that the formed He bubbles demonstrate diverse distribution feature and reduced bubble pressure at the hierarchical-interface in multi-layered $\text{Al}_{1.5}\text{CoCrFeNi}$ HEA films, suggesting that the homogeneous hierarchical-interfaces play a vital role in tailoring the distribution of He bubbles by increasing the bubble nucleation sites, which in turn mitigate the irradiation damage induced by He accumulation in the grains of each lamellae of HEA films. Partial phase transformation from body-centered-cubic (BCC) to face-centered-cubic (FCC) structure was triggered through promoting the structural evolution between irradiation-induced amorphous and compositional reorganization in these HEA films upon irradiation. The mechanisms behind irradiation-induced phase transformation were revealed by the bubble-pressure driven stress inside the lattice and the contribution of self-healing behavior around the irradiation-enhanced amorphous region.

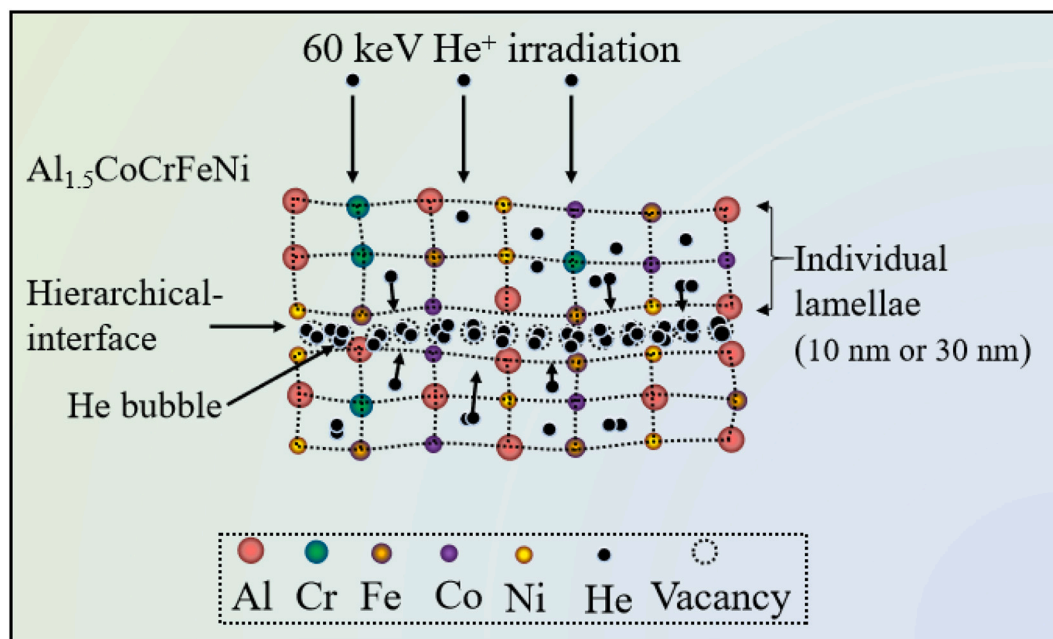


Fig. 1. The schematic diagram of $\text{Al}_{1.5}\text{CoCrFeNi}$ HEA multilayered structure (individual lamellae is 10 nm or 30 nm) with a homogeneous composition and stages of He introduction into hierarchical interfaces.

2. Experimental details

In the experimentation, the homogeneous multi-layered $\text{Al}_{1.5}\text{CoCrFeNi}$ HEA films with hierarchical-interfaces were deposited by RF magnetic sputtering technique at room temperature on about 1.65 mm thick single-crystalline silicon (Si) substrates. The detailed deposition parameters were described in reference [20]. The sputtering target composed of $\text{Al}_{1.5}\text{CoCrFeNi}$ was fabricated by powder metallurgy with high purity (>99.99%, weight percent) raw materials of aluminum, cobalt, chromium, iron, and nickel powders. In the two kinds of multi-layered films, the individual thickness in $\text{Al}_{1.5}\text{CoCrFeNi}$ layers is approximately 10 nm and 30 nm, respectively. These designed multi-layered structures could be briefly described as $[\text{Al}_{1.5}\text{CoCrFeNi} (10 \text{ nm})]_{30}$ and $[\text{Al}_{1.5}\text{CoCrFeNi} (30 \text{ nm})]_{10}$. The single-layer thickness was synthesized by closing damper alternately to disrupt deposition according to the fixed deposition time (26.5 s and 79.5 s, respectively) of each lamellae. Room temperature He^+ implantation experiments were then performed on the 60 keV platform at a fluence and a fluence rate of $1 \times 10^{17} \text{ cm}^{-2}$ and $5.56 \times 10^{13} \text{ cm}^{-2} \cdot \text{s}^{-1}$ to obtain depth profile of He distribution in the nano-multilayered $\text{Al}_{1.5}\text{CoCrFeNi}$ HEA films. The as-deposited HEA films were mounted on a water-cooling holder, and the ambient temperature was maintained around 300 K during irradiation.

The displacements per atom (DPA) and the He concentration as a function of depth were calculated by SRIM-2013 software with the full cascade TRIM simulation as the $\text{Al}_{1.5}\text{CoCrFeNi}$ HEA is multi-elemental target [27], using the threshold displacement energies of 25 eV for Al atom and 40 eV for other atoms as well as the $\text{Al}_{1.5}\text{CoCrFeNi}$ HEA density at 6.2449 g/cm^3 [28,29]. Grazing Incidence X-ray Diffraction (GIXRD, Bruker D8 Advanced) with a $\text{Cu K}\alpha$ radiation wavelength of 0.15418 nm was carried out to characterize the phase structure for the $[\text{Al}_{1.5}\text{CoCrFeNi} (10 \text{ nm})]_{30}$ and $[\text{Al}_{1.5}\text{CoCrFeNi} (30 \text{ nm})]_{10}$ multi-layered films before and after irradiation, the GIXRD data were recorded at a grazing incidence angle of 2° with a step of 0.03° and a dwell time of 3 s for each step. The cross-sectional morphology features in the irradiated HEA films with multilayered structure were characterized by the through-focused Bright Field Transmission Electron Microscope (BF-TEM, Tecnai G² F20). The Selected Area Electron Diffraction (SAED) was carried out to characterize the micro-structures of nano-multilayered $\text{Al}_{1.5}\text{CoCrFeNi}$ HEA films after He^+ irradiation. The cross-sectional TEM foils from the irradiated HEA films were prepared by mechanical polishing, followed by ion milling to form a wedge to create sufficient electron transparency on a Gatan precision ion polishing system.

3. Results

3.1. Bubble distribution features in the irradiated nano-multilayered HEA films

Fig. 2 shows the displacements per atom (DPA, values of irradiation damage) and He concentration as a function of depth in $\text{Al}_{1.5}\text{CoCrFeNi}$ HEA irradiated by 60 keV He^+ at fluence of $1 \times 10^{17} \text{ cm}^{-2}$. The profiles of DPA and He concentration with the depth present roughly Gaussian-like distribution. The variation of irradiation damage with depth indicate that the implanted depth is classified into three distinct regions: (I) a subsurface damage region of 150 nm depth, followed by (II) a damage peak region in the depth ranging from 150 nm to 275 nm in width, and finally (III) the less damaged region in HEA film. The maximum damage of irradiation region is roughly located at 225 nm in depth from the surface of sample, in which the calculated maximum values of DPA and He concentration are about 7.01 dpa and 7.42 at.% at fluence of $1 \times 10^{17} \text{ cm}^{-2}$, respectively. According to the simulation result, the real irradiation regions can be also certificated from the TEM images.

Fig. 3(a) shows the BF-TEM image of irradiated $[\text{Al}_{1.5}\text{CoCrFeNi} (10 \text{ nm})]_{30}$ multi-layered films. As shown in the cross-sectional micrograph, the damage feature as depth-profile (highlighted by yellow dotted line) also presents three conspicuous regions, which is in good

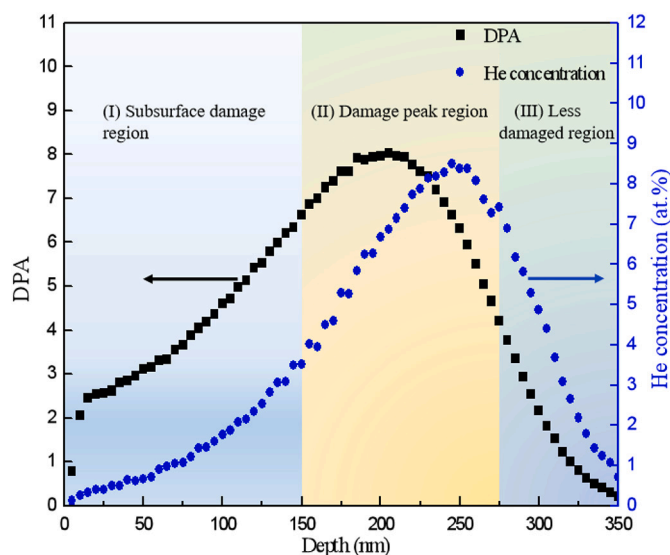


Fig. 2. The profiles of displacements per atom (dpa) and He concentration in $\text{Al}_{1.5}\text{CoCrFeNi}$ HEA as a function of depth for 60 keV He^+ at fluence of $1 \times 10^{17} \text{ cm}^{-2}$.

agreement with the calculated displacement damage profiles by SRIM. The numerous spherical He bubbles connected with ribbon-like structure are formed at the distinct interfaces of irradiated region, where hierarchical-interfaces provide enough defect sinks for He entrapment and bubble aggregation. It is worth to note that these He bubbles (remarked by black circles) agglomerated by the smaller He bubbles (remarked by red circles) or clusters are observed in the enlarged HRTEM image of Fig. 3(b). The inserted inverse Fast Fourier Transform (IFFT) image (shown in red rectangle) manifests that the lattice dislocations are produced due to the irradiation effect. Fig. 3(c) shows the amorphous regions and nano-crystal at irradiation damage peak region observed from the enlarged HRTEM image, as well as the inserted FFT and IFFT images (shown in red rectangles), indicating that the partial amorphous are induced on account of He bubble evolution. Fig. 3(d) presents the distribution of bubble size (the diameter of 2.4–5.1 nm), and the mean size of 3.8 nm is also calculated from the statistical data. At the same time, less He bubbles (marked by red circles) are detected in the nano-meter grains (~5–6 nm) of the $\text{Al}_{1.5}\text{CoCrFeNi}$ HEA films due to the existence of nano-crystals in each lamellae, suggesting that the introduced He atoms in lamellae matrix are mainly migrated into the interfaces through the diffusion channels of nano-GBs. Less bubble in each lamellae of HEA is attributed to the significant reduction of He concentration owing to the He migration into hierarchical-interfaces.

By reducing the number of interface, the similar spherical-bubbles connected with ribbon-like structure are also observed at the interfaces in irradiated $[\text{Al}_{1.5}\text{CoCrFeNi} (30 \text{ nm})]_{10}$ multi-layered films, as demonstrated in the Fig. 4(a). In addition, a part of He bubbles (marked by black circles) are also formed inside each lamellae, as illustrated in the corresponding HRTEM image of Fig. 4(b). Noteworthy, the grain sizes in multilayered film basically keep stable (~5–6 nm) even though the individual thickness increased from 10 nm to 30 nm. After He^+ irradiation, partial nano-crystals maintain their stability and integrity, as shown in the HRTEM and inserted IFFT images (in the red rectangle). Similarly, the amorphous regions are induced by He^+ irradiation in the film-layers, as shown in the enlarged HRTEM image (Fig. 4(c)), as well as the inserted FFT and IFFT images (shown in red rectangles). Compared with the bubble size in $[\text{Al}_{1.5}\text{CoCrFeNi} (10 \text{ nm})]_{30}$ multi-layered films, the distribution of smaller bubble (1.3–3.5 nm) and mean size (2.1 nm) are demonstrated in the $[\text{Al}_{1.5}\text{CoCrFeNi} (30 \text{ nm})]_{10}$ multi-layered films, as shown in the Fig. 4(d). Except for the bubble formation at interfaces, the implanted He atoms in each-lamellae are

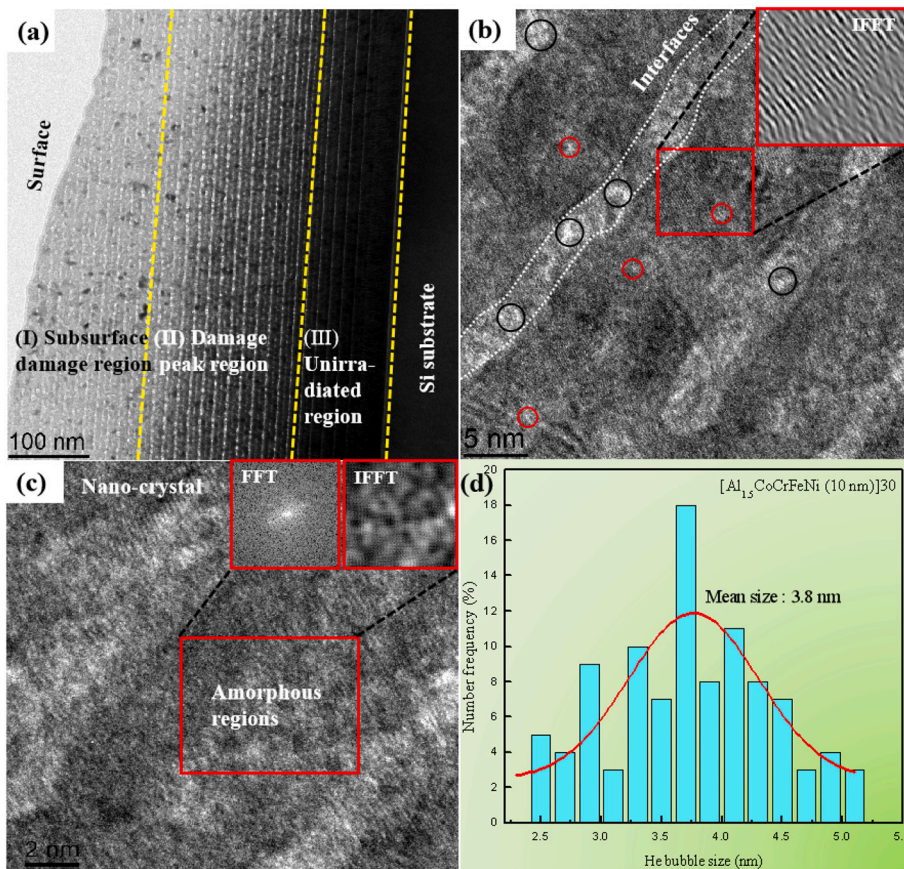


Fig. 3. (a) Cross-sectional micro-structure of $[\text{Al}_{1.5}\text{CoCrFeNi (10 nm)}]_{30}$ multi-layered HEA films irradiated by He^+ at room temperature with fluence of $1 \times 10^{17} \text{ cm}^{-2}$. (b) The corresponding enlarged HRTEM image obtained from the damage peak region, the inserted inverse FFT image transformed from HRTEM image. (c) The enlarged HRTEM image obtained from (b), in which amorphous regions were formed after He^+ irradiation, the FFT and IFFT images were also transformed from amorphous regions. (d) Size distribution of He bubbles in the $[\text{Al}_{1.5}\text{CoCrFeNi (10 nm)}]_{30}$ multi-layered HEA film irradiated at room temperature.

captured rapidly by the GBs in film matrix, then these He atoms are further aggregated to form bubbles inside each lamellae (marked by black circles). Also, the isolated He bubbles in the matrix, as well as He bubbles decorating GBs and dislocations were observed. He bubbles with ribbon-like structure are formed by the He-vacancy aggregation at GBs, indicating diffusion occurs readily along GBs and dislocations by a pipe diffusion mechanism. With increasing the nominal thickness of each-lamellae from 10 nm to 30 nm, and the nanocrystal is also enhanced correspondingly. Thus, the diffusion distance is considerably lengthened for He interstitials or vacancy defects diffusion from the original location to nearest interface sinks, enabling the rapidly diffused He atoms preferentially are trapped by the GBs in each lamellae, which is contributed to reducing bubble size. These phenomena demonstrate inverse results with previous modeling results that the more interfaces (smaller individual-layer thickness) play a crucial role in attracting of Frenkel pair defects and reducing bubble size for the dual-phase heterogeneous interfaces [28–31].

The coexistence of high-density nano-GBs inside each lamellae and hierarchical interfaces can account for the reduced bubble size in $[\text{Al}_{1.5}\text{CoCrFeNi (30 nm)}]_{10}$ multi-layered films, the bubble growth is delayed by increasing the nucleation density of bubble due to the coexistence of interfaces and GBs, which are generally viewed as preferred nucleation-site for bubbles. The formed He-vacancy complexes are expected instability and have a migration energy that can allow them to migrate and aggregate into bubbles [32], making for a wider bubble distribution with a smaller size and preferential He bubble formation at GBs in $[\text{Al}_{1.5}\text{CoCrFeNi (30 nm)}]_{10}$ nano-multilayered film. Previous investigation results also revealed smaller bubble size and superior bubble formation resistance in FeNiCoCr HEA compared with the pure nickel under the same condition because of the sluggish He diffusion in HEA [11]. Moreover, K.Y. Tsai et al. [33] reported that the high activation energy and low atomic diffusion mobility result from the

significant atomic traps and blocks in CoCrFeMnNi HEA due to the greater fluctuation of lattice potential energy. Although there is a distinct discrepancy between solute atomic diffusion and He interstitial diffusion on account of its very low solubility and ability of forming bubble, the sluggish diffusion effect and high activation energy can also provide evidence for the hysteresis growth of He bubble at interfaces and inside each lamellae of $[\text{Al}_{1.5}\text{CoCrFeNi (30 nm)}]_{10}$ multi-layered films.

3.2. He bubble pressure in the irradiated nano-multilayered HEA films

Fig. 5 shows the pressure inside bubbles in the $\text{Al}_{1.5}\text{CoCrFeNi}$ HEA nano-multilayered films at the irradiated region. At thermodynamic equilibrium, the pressure (P) inside a bubble is expected to be approximately calculated by the following equation [34]:

$$P = 2\gamma_{sv}/r \quad (1)$$

where γ_{sv} is the surface free energy and r is the bubble radius. The surface energy γ_{sv} for the $\text{Al}_{1.5}\text{CoCrFeNi}$ HEA is estimated to be about $1.8103 \text{ J}\cdot\text{m}^{-2}$, which is calculated by averaging the surface energy of each element, the detailed surface energy of each element [35] is listed in Table 1. Bubble pressures of 0.71–2.79 GPa are approximately quantified from the detectable bubbles' diameters of ~ 1.2 – 5.0 nm. The calculated pressures are close to the equilibrium pressure at the He peak concentration of ~ 7.42 at.% implanted at depth of 250 nm. In addition, the data of bubble pressure obtained from Ni [36], $\text{Ni}_{80}\text{Cr}_{20}$ [37], FeCoCrNi [38] and FeCoCrNiMn [39] bulk materials are also contrasted, then their bubble pressures are over-pressurized under the analogical He^+ irradiation environment. Higher surface energy as well as smaller bubble size are contributed to enhance the bubble pressure in these bulk materials. Especially, the reduced pressures inside bubbles are demonstrated in the $\text{Al}_{1.5}\text{CoCrFeNi}$ HEA nano-multilayered films, in which a

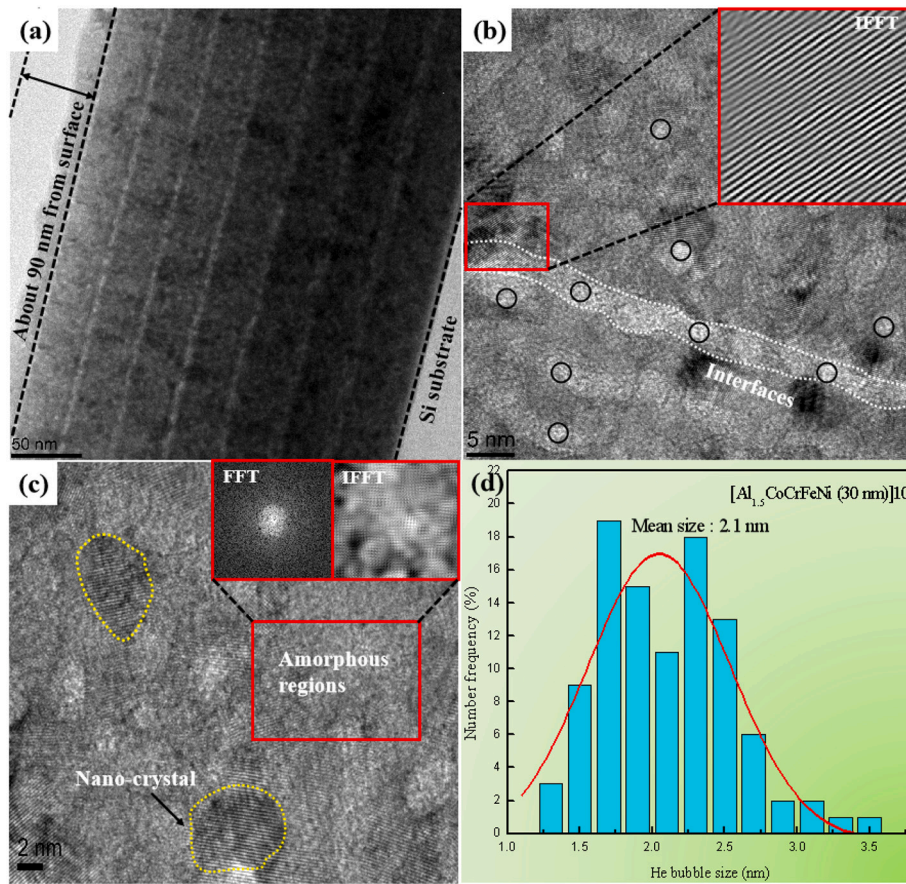


Fig. 4. Cross-sectional micro-structure of $[\text{Al}_{1.5}\text{CoCrFeNi (30 nm)}]_{10}$ multi-layered HEA films irradiated by He^+ at room temperature with fluence of $1 \times 10^{17} \text{ cm}^{-2}$. (b) The corresponding enlarged HRTEM image obtained from the damage peak region, the inserted inverse FFT image transformed from HRTEM image. (c) The enlarged HRTEM image obtained from (b), in which amorphous regions were formed after He^+ irradiation, the FFT and IFFT images were also transformed from amorphous regions. (d) Size distribution of He bubbles in the $[\text{Al}_{1.5}\text{CoCrFeNi (30 nm)}]_{10}$ multi-layered HEA film irradiated at room temperature.

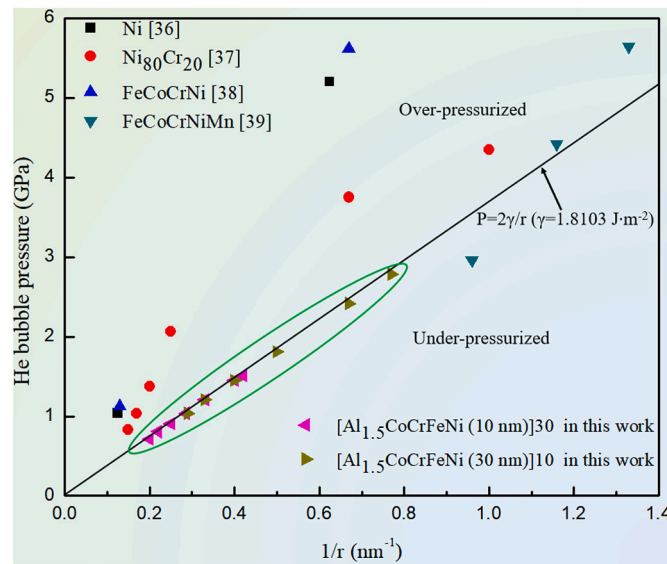


Fig. 5. The pressure inside He bubbles in the $[\text{Al}_{1.5}\text{CoCrFeNi (10 nm)}]_{30}$ and $[\text{Al}_{1.5}\text{CoCrFeNi (30 nm)}]_{10}$ nano-multilayered HEA film as a function of the inverse radius. Data of bubble pressure obtained from Ni [36], NiCr [37], FeCoCrNi [38] and FeCoCrNiMn [39] were also contrasted.

lower surface energy and multilayered interface are contributed to the reduced pressure inside bubble in comparison with those binary, ternary alloys or FeCoCrNiMn HEAs. A specific relation can be defined between the number of He atoms in a bubble and its radius by establishing bubble models. We use the idea gas law to describe the thermodynamic state of

Table 1

The surface energy γ_{SV} of all elements [35].

Element	Al	Co	Cr	Fe	Ni
Surface energy ($\gamma_{SV}/(\text{J}\cdot\text{m}^{-2})$)	1.020	2.218	2.006	2.123	2.080

He in bubbles [40]. Supposing n_x to be the number of gas atoms in a spherical bubble of radius r , then:

$$PV = nkT \quad (2)$$

Eq. (3) can be derived by combining equation Eqs. (1) and (2):

$$n_x = 4 \left/ 3\pi r^3 \frac{2\gamma}{rkT} = \frac{8\pi r^2 \gamma}{3kT} \quad (3)$$

where the k is boltzmann constant ($k = 1.3806 \times 10^{-23} \text{ J/K}$) and T is irradiation temperature (about 298 K). The estimated number of He atoms n_x are in the range of $\sim 5.31 \times 10^3$ – 9.22×10^4 in these bubbles based on the bubble diameters of ~ 1.2 – 5.0 nm .

3.3. Phase structure evolution in the irradiated nano-multilayered HEA films

Figs. 6(a) and (b) show the GIXRD patterns of $\text{Al}_{1.5}\text{CoCrFeNi}$ HEA multi-layered films before and after He^+ irradiation. The patterns were abstracted from the diffraction angle ranging from 40° to 48° . The phase composition presents a BCC single-phase structure in the unirradiated HEA films. From the fitting curves in patterns, except for the BCC (110) diffraction peak, FCC (111) diffraction peak can be both observed in the irradiated $[\text{Al}_{1.5}\text{CoCrFeNi (10 nm)}]_{30}$ and $[\text{Al}_{1.5}\text{CoCrFeNi (30 nm)}]_{10}$ nano-multi-layered films, this result indicates that the partial phase

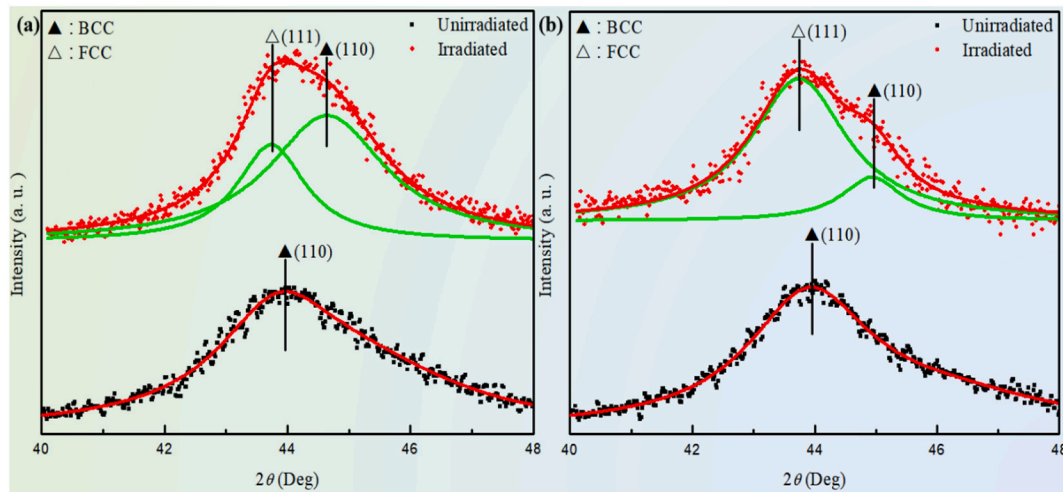


Fig. 6. GIXRD patterns of nano-multilayered HEA film (a) $[\text{Al}_{1.5}\text{CoCrFeNi} (10 \text{ nm})]_{30}$ and (b) $[\text{Al}_{1.5}\text{CoCrFeNi} (30 \text{ nm})]_{10}$ before and after irradiated at $1 \times 10^{17} \text{ cm}^{-2}$.

transformation from BCC to FCC structure in these nano-multilayered HEA films is induced by He^+ irradiation. The FCC phase volume fractions V_f approximate 43.46% and 76.52%, respectively, which are roughly estimated based on the integrated intensity (I) values of the deconvoluted GIXRD peaks as follows [41]:

$$V_f(\%) = \frac{I_{\text{fcc}(111)}}{I_{\text{fcc}(111)} + I_{\text{bcc}(110)}} \times 100\% \quad (4)$$

M. Barr et al. [42] reported the radiation induced segregation (RIS) at high angle grain boundaries in the CoCrFeNiMn HEA under irradiation damage level of 2–3 dpa. The RIS behavior is known to be a redistribution of solute atoms induced by irradiation-induced enrichment or depletion, the segregated alloy atom results in an element concentration that exceeding the solubility limit, and finally inducing the formation of secondary phases [43]. Therefore, it may be predicted that the interaction of irradiation defects and interfaces in the designed multi-layered $\text{Al}_{1.5}\text{CoCrFeNi}$ HEA films would induce phase transformation under this irradiation damage level. The aggregation of He bubbles in film matrix may be promotes the enhanced V_f in the irradiated $[\text{Al}_{1.5}\text{CoCrFeNi} (30 \text{ nm})]_{10}$ multilayered films. Also, the bubble-pressure driven stress offers a dynamic for the compositional reorganization and partial FCC phase formation. With tailoring the interface number, the volume fraction of the FCC and BCC phases in the laminate structure change correspondingly, thus achieving tailored mixtures of hard BCC and ductile FCC phases, meanwhile the density of the phase boundaries is also optimized to tuning bubble distribution within each nanocrystalline grain. Furthermore, the peak position and full width at half maximum (FWHM) of these films are tabulated in Table 2. In contrast to the unirradiated HEA films, the BCC (110) peaks of the irradiated film continuously shift to higher diffraction angles, suggesting

the decrease of the corresponding interplanar distance for each lamellae after ion irradiation, the interplaner distance shrinkage is resulted from residual compression-stress, which is induced by the growth of He bubble at interfaces or inside crystals. It is consistent with the results that the lattice disorder and partial amorphous regions (as shown in Fig. 3 and Fig. 4) are induced by the irradiation-enhanced strain. Especially, the significant variations in FWHM of BCC (110) peak and intensity of FCC (111) peak indicate the irradiation-induced FCC transformation from the original BCC phase and the increase of corresponding grain size.

Fig. 7(a) shows the HRTEM image of $[\text{Al}_{1.5}\text{CoCrFeNi} (10 \text{ nm})]_{30}$ multi-layered films, in which both nano-crystalline structure and irradiation-induced amorphous regions are observed near the interfaces. Irradiation-induced amorphous region is further presented in HRTEM, FFT and IFFT images, as shown in Fig. 7(b). Fig. 7(c) displays the SAED pattern of $[\text{Al}_{1.5}\text{CoCrFeNi} (10 \text{ nm})]_{30}$ nano-multilayered films. SAED pattern is obtained from the damage peak regions to further certificate the phase evolution. Except for the initial BCC phase in diffraction loops, FCC (111), FCC (200) and FCC (220) diffraction loops are also formed in the SAED pattern. The d -spacing ($d_{(110)} = 0.2035 \text{ nm}$, $d_{(111)} = 0.1982 \text{ nm}$) and corresponding grain orientation are given in the IFFT images (Figs. 7(d) and (e)), which are transformed from the HRTEM image of the damage peak region A and B, as shown in black and red rectangles in Fig. 7(a), respectively. The measured d -spacing is basically consistent with the calculated values ($d_{(110)} = 0.2030 \text{ nm}$, $d_{(111)} = 0.2070 \text{ nm}$) from GIXRD patterns (The Fig. 6), the slight error in d -spacing may be derived from the lattice distortion induced by the He atoms. According to the above analysis results, partial phase transformation from BCC to FCC structure is induced under the induction effect of the partial amorphous formation and internal strain, which are induced due to the introduction of He-vacancy complexes and bubbles, etc. The remission and transmission of irradiation-enhanced strain are responsible for the phase transformation through the structural evolution between the partial amorphous formation and compositional reorganization upon irradiation [44,45]. Besides, The phase transformation originated from the RIS behavior is also tightly associated with the diffusion behavior of solute or solvent atoms, which will be elaborated in the following discussion part.

4. Discussion

4.1. The bubble evolution mechanism in nano-multilayered HEA films

The distinctive distribution of He bubble is identified in

Table 2

The parameters of peak position and FWHM in $\text{Al}_{1.5}\text{CoCrFeNi}$ HEA multilayered films before and after He^+ irradiation.

Samples	(110) peak position	(111) peak position	(110) FWHM	(111) FWHM
$[\text{Al}_{1.5}\text{CoCrFeNi} (10 \text{ nm})]_{30}$ (unirradiated)	43.8542	–	2.3834	–
$[\text{Al}_{1.5}\text{CoCrFeNi} (10 \text{ nm})]_{30}$ (irradiated)	44.6447	43.7363	2.3090	1.3531
$[\text{Al}_{1.5}\text{CoCrFeNi} (30 \text{ nm})]_{10}$ (unirradiated)	43.9148	–	2.4689	–
$[\text{Al}_{1.5}\text{CoCrFeNi} (30 \text{ nm})]_{10}$ (irradiated)	44.9365	43.7433	1.2113	1.8905

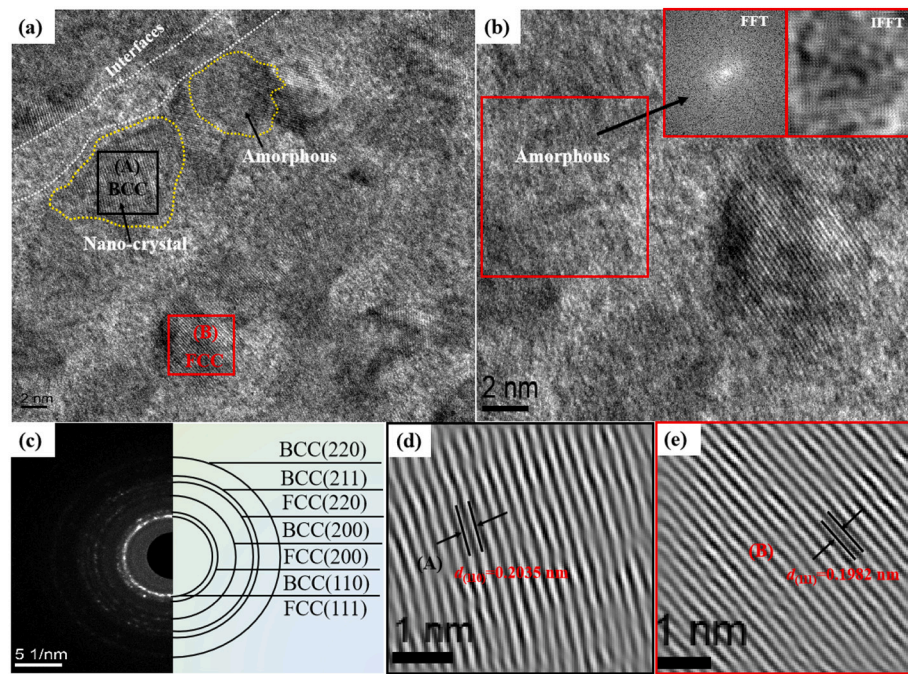


Fig. 7. (a) The HRTEM image of $[\text{Al}_{1.5}\text{CoCrFeNi (10 nm)}]_{30}$ nano-multilayered HEA film. (b) The HRTEM image of amorphous region, the inserted FFT and IFFT images transformed from amorphous region; (c) The SAED pattern obtained from the damage peak region; (d) and (e) the IFFT images transformed from the (A) and (B) region in (a).

$[\text{Al}_{1.5}\text{CoCrFeNi (10 nm)}]_{30}$ and $[\text{Al}_{1.5}\text{CoCrFeNi (30 nm)}]_{10}$ nano-multilayered films, indicating that the high-density hierarchical-interfaces play a vital role in storing He atoms and reducing bubble size. The recombination effect between radiation-induced interstitials and vacancies at the interfaces and nano-GBs may be responsible for the radiation tolerance. Molecular dynamics simulation results have revealed that the collision cascade produced vacancies and interstitials are easily captured into the hierarchical-interfaces [24], the nano-crystals in each lamellae possess a more excellent radiation tolerance because of the greater concentration of GBs [21–23]. In the $\text{Al}_{1.5}\text{CoCrFeNi}$ HEA nano-multilayered films, the irradiation-induced defects including vacancies, He interstitials and self-interstitials could be easily moved to the high-density hierarchical-interfaces or GBs, then these irradiated defects can annihilate each other (inter-annihilation may occur). A combination of He atoms and vacancy-type defects precipitates into He clusters, then evolves into spherical He bubbles above a critical He concentration at the surrounding of interfaces [46]. Furthermore, with increasing individual thicknesses from 10 nm to 30 nm in nano-multilayered HEA films, the interface number reduce while the nano-GBs increase inside each film-layer simultaneously. More GBs can disperse He distribution in each-lamellae of film matrix, suppressing the dramatic growth for bubbles. Accordingly, the synergistic effect of interface and GB enables the storage of He atom in a stable manner and reduces the probability of “bubble-to-void” transformation. As a result, formation of He bubbles is retarded and the growth rate as well as migration of the bubbles can be reduced due to the coexistence of nano-crystals and hierarchical-interfaces. Noteworthy, the distribution characteristic of bubble demonstrates inverse results with previous modeling results that the more interfaces (smaller individual-layer thickness) offer more nucleation sites for He bubble. In the $[\text{Al}_{1.5}\text{CoCrFeNi (30 nm)}]_{10}$ nano-multilayered film, the implanted He can be dispersed and the critical fluence of implanted He in alloys required to transform stable bubbles into voids could be enhanced by the synergistic effect of GBs and hierarchical-interfaces.

From the perspective of differing atomic-level structures, abundant vacancies are introduced at interfaces, which are regarded as the preferred sites for He entrapment and nucleation of He bubble [26]. The

previous simulation results have disclosed that the He atoms and vacancies precipitate into relatively flat He platelets due to the non-uniform, location-dependent interface energy and the special characteristic of interface atom mismatch [47]. Therefore, a mass of He-vacancy complexes are aggregated into nano-meter He bubbles rather than large-scale cavities or voids. As shown in Fig. 3 and Fig. 4, the influence of the interface on He bubble distribution and size is certificated by tailoring the individual-thickness of each lamellae. The calculated mismatch in atom size in the $\text{Al}_{1.5}\text{CoCrFeNi}$ HEA films ranges from 1.9% to 9.7% based on the equations below [28]:

$$\Delta R = (R_i - R_a)/R_a \quad (5)$$

$$R_a = \sum_{i=1}^n R_i C_i \quad (6)$$

where R_a is the average atomic radius, R_i is atomic radius of component and C_i is the molar percent of component. The atom difference is intimately associated with the lattice mismatch at hierarchical interface of $\text{Al}_{1.5}\text{CoCrFeNi}$ HEA nano-multilayered films. Previous results have also revealed that these critical He concentrations in multilayered films depend on the lattice parameter difference, which closely matches that of the increase of vacancy concentration and He bubble nuclei density [49]. In this work, more interfaces in $[\text{Al}_{1.5}\text{CoCrFeNi (10 nm)}]_{30}$ nano-multilayered film can trap He atoms to form small bubble, these bubble further evolve into large-sized bubble with ribbon-like structure due to the enhanced vacancy concentration and He bubble nuclei density. The bubble or bubble nuclei may be controlled with a desired interface density by tailoring the lamellae spacing [48,49]. The optimized interface density achieves desired behavior, e.g. the He entrapment or the He stable storage at hierarchical-interface may be also tuned.

4.2. The reduced bubble pressure in nano-multilayered HEA films

In contrast to the over-pressured bubble in binary or ternary alloys, the bubble growth and reduced bubble pressure in nano-multilayered HEA films mainly can be put down to the lower surface energy and

interface number. Kashinath et al. established the bubble growth evolution mode by interface wetting [24]. Because of lower surface free energy of the solid materials, the He clusters or bubbles — much like a water drop on a glass surface — can not be well wetting with the interface. The reduced surface energy of Al_{1.5}CoCrFeNi HEA is beneficial to the nano-meter bubble in a stable storage at interfaces. Compared with high surface energy in Ni, Ni₈₀Cr₂₀, FeCoCrNi and FeCoCrNiMn bulk materials, the inferior wetting ability in Al_{1.5}CoCrFeNi HEA multilayered films can suppress those unstable nano-meter bubbles diffusing into the both sides of film layer due to the bubble with a low contact area, while the bubbles in those bulk materials may be transformed into large-sized bubble or nano-voids due to their special growth-model. The numerous spherical He bubbles connected with ribbon-like structure, indicating that the bubbles diffuse along the horizontal direction of interplanar to change the growth mode. Similarly, the implanted He atoms were evolved into stable He platelets rather than bubbles to decrease rates of coarsening and coalescence based on the multi-scale modeling result [26], then changing the bubble distribution in nano-multilayered films at a certain point. Slightly reduced bubble pressure is calculated in the [Al_{1.5}CoCrFeNi (10 nm)]30 nano-multilayered film due to the bubble pressure is inversely proportional to its size, suggesting that the increase of interface number is a main controlling factor in increasing bubble size rather than internal pressure. In comparison with the bubble pressure in those bulk materials, a smaller bubble pressure is tuned by the hierarchical-interface in multilayered HEA films, suggesting that the interfaces and nano-GBs play a crucial role in reducing bubble size and delaying the “bubble-to-void” transformation by increasing the bubble nucleation sites, which in turn mitigate the irradiation damage induced by the He accumulation in grains of HEA film matrix.

4.3. Phase transformation mechanism in nano-multilayered HEA films

The introduction of nano-crystal and hierarchical-interface is responsible for irradiation-induced partial BCC → FCC phase transformation in the Al_{1.5}CoCrFeNi HEA nano-multilayered films. Thus, a phase transition in these irradiated Al_{1.5}CoCrFeNi HEA nano-multilayered films can occur when the thermodynamic equation satisfies following modified condition according to the thermodynamic free energy effects [50]:

$$\Delta G_{hi} + \Delta G_{gb} + \Delta G_{id} > \Delta G_{pt} \quad (7)$$

where ΔG_{hi} is the Gibbs free energy of hierarchical-interface, ΔG_{gb} is the Gibbs free energy of grain boundaries, ΔG_{id} is the Gibbs free energy of irradiation defects (including point defects and He bubbles), and ΔG_{pt} is the Gibbs free energy barrier for the phase transition. Assuming that the grains are spherical and have grain size (diameter) d and molar volume V_m , the Gibbs free energy of grain boundaries is given by Ref. [50]:

$$\Delta G_{gb} = \frac{3V_m\sigma}{d} \quad (8)$$

where σ is the specific Gibbs free energy of the grain boundary. ΔG_{gb} is inversely proportional to grain size d ($\Delta G_{gb} \sim 1/d$). Because ΔG_{gb} and ΔG_{id} are proportional to $1/d$ [51,52] and d^2 [53] respectively (d meaning the grain size), there could exist an inverse evolution between ΔG_{gb} and ΔG_{id} when the grain size d decreases or increases. The larger He bubble size can stimulate the increase in ΔG_{hi} and ΔG_{id} due to the high-density interfaces in the irradiated [Al_{1.5}CoCrFeNi (10 nm)]30 nano-multilayered film. For the irradiated [Al_{1.5}CoCrFeNi (30 nm)]10 nano-multilayered film, the increase of ΔG_{gb} and ΔG_{id} may prompt phase transition on account of the GBs increase and bubble distribution at interface and inside film matrix simultaneously.

Irradiation-induced disorder and amorphous regions are detected in the HRTEM images (Fig. 3 and Fig. 4). To clearly elucidate the microstructure evolution of Al_{1.5}CoCrFeNi HEA multi-layered films upon

irradiation, the schematic illustration is shown in Fig. 8. As the introduction of irradiation-induced He defects, the lattice disorder is increased accordingly. Irradiation-enhanced strain can give rise to the propagation of defects and facilitate their motion, afterwards resulting in partial amorphous at the irradiated region under the extreme high strain field. Irradiation-induced disorder aggravates the negative heats of formation, and the disruption of chemical short-range order will lead to lattice destabilization or the formation of an amorphous phase [54]. However, the irradiation-induced strain cannot increase infinitely and the strain release occurs gradually accompanied by the He atom and vacancy migration into hierarchical-interface. Interdiffusion and exchange between the defect flux and HEA atoms are responsible for the compositional reorganization based on an inverse Kirkendall effect (i.e. vacancy or interstitial flux in the opposite direction of net solute flux) [55]. Moreover, the implanted He⁺ kinetic energy is certainly transferred to the primary knock-on atoms (PKAs), and their mean free path is so short that their energy might be dissipated within a region of 5–10 nm in a time less than 1 p-second, initiating a thermal spike (TS) [56]. In the irradiated Al_{1.5}CoCrFeNi HEA multi-layered films, aforementioned cascade-induced thermal spike also induces the grain growth and the transformation of short-range order from the disorder regions [6]. As well known that the ordered state comes from the arrangement of atoms and minimizes the free energy of the solid materials [57]. Irradiation-induced disorder increases the free energy of the solid materials above the equilibrium value. Hence, a new free energy balance may be achieved between adjacent phases in the alloy under irradiation conditions. The ordered structure transformation from amorphous region can release the interior compression-stresses developed near the He bubble defects in crystals of nano-multilayered HEA films. The process of stress release may act as driving force to promote the composition reorganization and partial FCC phase transformation from the original BCC matrix.

The FCC phase transformation results from the irradiation-induced diffusion and segregation behavior in HEAs. To understand the diffusion behavior in these multilayered films, the diffusion kinetics mechanism of alloy atoms is proposed to account for the phase transformation. In general, the defects are more loosely bounded among the lattice atoms, the lower activation energy and the higher diffusion coefficient expedite the alloy atom enrichment or depletion [58]. Therefore, interface or GBs diffusion of alloy atom requires a lower activation energy than that for other forms of diffusion since each surface atom has only half the nearest neighbors as it does in the bulk, and generally [58]:

$$\bar{D} = D_a^v \exp\left(\frac{-Q_a^v}{kT}\right) + D_{gb} \exp\left(\frac{-Q_{gb}}{kT}\right) \quad (9)$$

where D_a^v and Q_a^v refer to vacancy self-diffusion and D_{gb} and Q_{gb} refer to GB diffusion. In most metals, $Q_a^v \sim 2Q_{gb}$. So, the GB diffusion plays a dominated role at low temperature, and at high temperature, alloy atom diffusion is dominated by bulk or volume diffusion. The GB dominated diffusion-behavior prompts the spatial redistribution of solute or solvent atoms in irradiated Al_{1.5}CoCrFeNi HEA nano-multilayered films. M. Vaidya et al. [59,60] found the diffusivities following the order $D_{Cr} > D_{Fe} > D_{Co} > D_{Ni}$ in CoCrFeNi multi-principal element alloy by using the radiotracer method. The Al atom has much lower activation energy of self-diffusion (142.0 kJ·mol⁻¹) and thus decreases the average level of activation energy of diffusion in the lattice of Al_{1.5}CoCrFeNi HEA [61]. Also, the irradiation-induced phenomena of Co, Ni depletion and Al, Fe, Cr enrichment at irradiated regions have been revealed in previous studies [62,63], causing a nonuniform distribution of alloy atom due to the irradiation-induced segregation. Similarly, the irradiation-induced partial BCC → FCC phase transformation and element segregation were disclosed by low energy and high fluence He⁺ induced vacancy-type defects in Al_{1.5}CrFeNi films, and the remarkable diffusion and segregation of the alloy elements were elucidated in detailed [62]. Yang

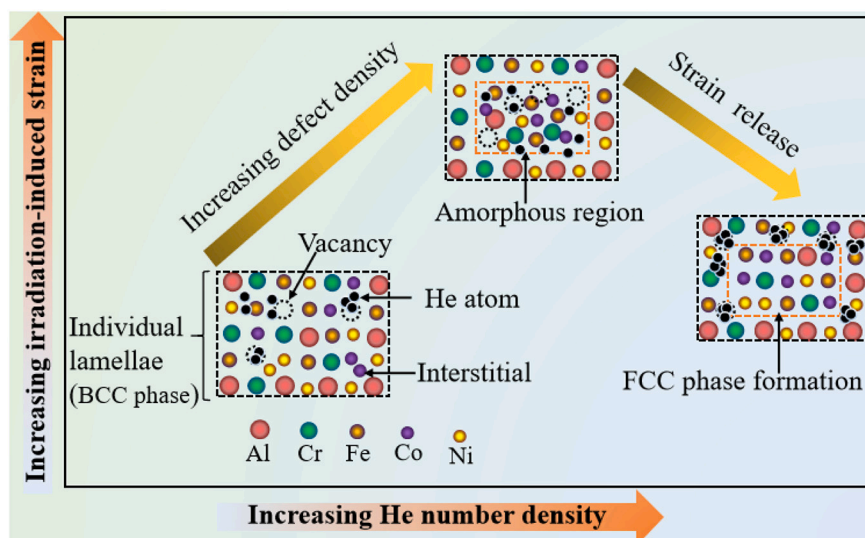


Fig. 8. The schematic diagram of micro-structural evolution inside individual lamellae of $\text{Al}_{1.5}\text{CoCrFeNi}$ HEA multilayered film during He^+ irradiation process at fluence of $1 \times 10^{17} \text{ cm}^{-2}$.

et al. [64] revealed that the FCC phase is enriched in Fe, Cr and Co, while the BCC phases are enriched in Al and Ni due to the different negative formation enthalpy between the BCC and FCC structure. Consequently, the diffusion-driven segregation of alloying elements exceeds the solubility limit and induces partial FCC phase formation in the irradiated regions of $\text{Al}_{1.5}\text{CoCrFeNi}$ nano-multilayered HEA films.

5. Conclusion

In summary, the hierarchical-interfaces were obtained in the homogeneous $[\text{Al}_{1.5}\text{CoCrFeNi} (10 \text{ nm})]_{30}$ and $[\text{Al}_{1.5}\text{CoCrFeNi} (30 \text{ nm})]_{10}$ nano-multilayered films, in which each-lamellae was composed of nano-meter grain to explore the coexistence of interfaces and GBs on the He^+ irradiation-induced micro-structural evolution and phase transformation behavior systematically. Results indicated that the He bubbles size in multilayered film exhibited reduction tendency and a wide distribution feature as the individual-thickness is increased from 10 nm to 30 nm. While higher bubble pressures were measured in the multilayered film with individual-thickness of 30 nm due to the reduced interfaces, indicating that the tuned interfaces and nano-meter GBs density at hierarchical-interfaces were beneficial to manage He distribution and delayed bubble growth effectively by tailoring the each-lamellae size inside HEA films. Partial phase transformation from BCC to FCC structure was revealed by promoting the structural evolution between the irradiation-induced amorphous and compositional reorganization in these HEA films upon irradiation, thereby enhancing the high recombination rate for the annihilation of these defects. The coexistence of interfaces and GBs promoted the annihilation of these defects and further facilitated the self-healing behavior in these $\text{Al}_{1.5}\text{CoCrFeNi}$ HEA nano-multilayered films.

CRediT authorship contribution statement

Guo Pu: Conceptualization, Methodology, Investigation, Formal analysis, Writing – original draft, Writing – review & editing. **Qiran Li:** Supervision. **Jia Li:** Supervision. **Sheng Chen:** Writing – review & editing. **Kun Zhang:** Methodology, Investigation, Writing – review & editing. **Chi Yang:** Writing – review & editing, Resources. **Zhijun Wang:** Supervision. **Liwei Lin:** Software, Formal analysis, Funding acquisition. **Ding Ren:** Conceptualization, Supervision. **Zongbiao Ye:** Supervision. **Bin Liu:** Writing – review & editing, Resources. **Bo Liu:** Methodology, Resources, Writing – original draft, Writing – review & editing,

Supervision, Funding acquisition.

Declaration of competing interest

The authors declare that they have no known competing financial interests or personal relationships that could have appeared to influence the work reported in this paper.

Acknowledgments

This work was supported by the National Key Research and Development Program of China (Grant 2018YFA0702100), NSAF Joint Fund (Grant No. U2130115) and the National Natural Science Foundation of China, China (Grant No. 11605116).

References

- [1] J.W. Yeh, S.K. Chen, S.J. Lin, J.Y. Gan, Nanostructured high-entropy alloys with multiple principal elements: novel alloy design concepts and outcomes, *Adv. Eng. Mater.* 6 (2004) 299–303.
- [2] H. Jiang, D.X. Qiao, W.N. Jiao, K.M. Han, Y.P. Lu, P.K. Liaw, Tensile deformation behavior and mechanical properties of a bulk cast $\text{Al}_{0.9}\text{CoFeNi}_2$ eutectic high-entropy alloy, *J. Mater. Sci. Technol.* 61 (2021) 119–124.
- [3] W.Y. Chen, M.A. Kirk, N. Hashimoto, J.W. Yeh, X. Liu, Y.R. Chen, Irradiation effects on $\text{Al}_{0.3}\text{CoCrFeNi}$ and CoCrMnFeNi high-entropy alloys, and 316H stainless steel at 500°C , *J. Nucl. Mater.* 539 (2020), 152324.
- [4] S.J. Zhao, Defect properties in a VTaCrW equiatomic high entropy alloy (HEA) with the body centered cubic (bcc) structure, *J. Mater. Sci. Technol.* 44 (2020) 133–139.
- [5] Q. Xu, H.Q. Guan, Z.H. Zhong, S.S. Huang, J.J. Zhao, Irradiation resistance mechanism of the CoCrFeMnNi equiatomic high-entropy alloy, *Sci. Rep.* 11 (2021) 608.
- [6] J.R. Zhou, M.I. Islam, S.M. Guo, Y. Zhang, F.Y. Lu, Radiation-induced grain growth of nanocrystalline AlxCoCrFeNi high-entropy alloys, *J. Phys. Chem. C* 125 (2021) 3509–3516.
- [7] L. Jiang, Y.J. Hu, K. Sun, P.Y. Xiu, M. Song, Y.W. Zhang, W.L. Boldman, M. L. Cresillo, P.D. Rack, L. Qi, W.J. Weber, L.M. Wang, Irradiation-induced extremes create hierarchical face-/body-centered-cubic phases in nanostructured high entropy alloys, *Adv. Mater.* 2002652 (2020).
- [8] M.A. Tunes, G. Greaves, H. Bei, P.D. Edmondson, Y. Zhang, S.E. Donnelly, C. G. Schon, Comparative irradiation response of an austenitic stainless steel with its high-entropy alloy counterpart, *Intermetallics* 132 (2021), 107130.
- [9] Z.J. Zhang, E.H. Han, C. Xiang, Irradiation behaviors of two novel single-phase bcc-structure high-entropy alloys for accident-tolerant fuel cladding, *J. Mater. Sci. Technol.* 84 (2021) 230–238.
- [10] N. Hashimoto, T. Fukushi, E. Wada, W.-Y. Chen, Effect of stacking fault energy on damage microstructure in ion-irradiated CoCrFeNiMn concentrated solid solution alloys, *J. Nucl. Mater.* 545 (2021), 152642.
- [11] W.T. Lin, D. Chen, C.Q. Dang, P.J. Yu, G. Wang, J.H. Lin, F.L. Meng, T. Yang, Y. L. Zhao, S.F. Liu, J.P. Du, G.M. Yeli, C.T. Liu, Y. Lu, S. Ogata, J.J. Kai, Highly

- pressurized helium nano-bubbles promote stacking-fault-mediated deformation in FeNiCoCr high-entropy alloy, *Acta Mater.* 210 (2021), 116843.
- [12] J.T. Hu, J.W. Zhang, J.J. Zhang, H.Y. Xiao, L. Xie, H.H. Shen, P.C. Li, G.A. Sun, X. T. Zu, Theoretical combined experimental study of unique he behaviors in high-entropy alloys, *Inorg. Chem.* 60 (2021) 1388–1397.
 - [13] Z.B. Zhu, H.F. Huang, O. Muránsky, J.Z. Liu, Z.Y. Zhu, Y. Huang, On the irradiation tolerance of nano-grained ni-mo-cr alloy: 1 MeV He+ irradiation experiment, *J. Nucl. Mater.* 544 (2021), 152694.
 - [14] Z.F. Yan, S.S. Liu, S.Q. Xia, Y. Zhang, Y.G. Wang, T.F. Yang, He behavior in Ni and Ni-based equiatomic solid solution alloy, *J. Nucl. Mater.* 505 (2018) 200–206.
 - [15] L.K. Mansur, W.A. Coghlan, Mechanisms of helium interaction with radiation effects in metals and alloys -a review, *J. Nucl. Mater.* 119 (1983) 1–25.
 - [16] R.E. Stoller, G.R. Odette, Analytical solutions for helium bubble and critical radius parameters using a hard-sphere equation of state, *J. Nucl. Mater.* 131 (1985) 118–125.
 - [17] M. Epanovi, V.D. Castro, I. García-Cortés, F.J. Sánchez, T. Leguey, Characterisation of open volume defects in Fe-Cr and ODS Fe-Cr alloys after He+ and Fe+ ion irradiations, *J. Nucl. Mater.* 538 (2020), 152230.
 - [18] E.Y. Lu, I. Makkonen, K. Mizohata, Z.M. Li, J. Räisänen, F. Tuomisto, Effect of interstitial carbon on the evolution of early-stage irradiation damage in equiatomic FeMnNiCoCr high-entropy alloys, *J. Appl. Phys.* 127 (2020), 025103.
 - [19] L.J. Beyerlein, M.J. Demkowicz, A. Misra, B.P. Uberuaga, Defect-interface interactions, *Prog. Mater. Sci.* 74 (2015) 125–210.
 - [20] G. Pu, L.W. Lin, R. Ang, K. Zhang, B. Liu, B. Liu, T. Peng, S.F. Liu, Q.R. Li, Outstanding radiation tolerance and mechanical behavior in ultra-fine nanocrystalline Al_{1.5}CoCrFeNi high entropy alloy films under he ion irradiation, *App. Sur. Sci.* 516 (2020), 146129.
 - [21] F.D. Chen, X.B. Tang, H. Huang, X.X. Li, Y. Wang, C.Q. Huang, J. Liu, H. Li, D. Chen, Formation of he-rich layers observed by neutron reflectometry in the he-ion-irradiated Cr/W multilayers: effects of Cr/W interfaces on the he-trapping behavior, *ACS Appl. Mater. Inter.* 8 (2016) 24300–24305.
 - [22] X.Y. Liu, B.P. Uberuaga, M.J. Demkowicz, et al., Mechanism for recombination of radiation-induced point defects at interphase boundaries, *Phys. Rev. B* 85 (2012), 012103.
 - [23] X. Zhang, N. Li, O. Anderoglu, H. Wang, J.G. Swadener, T. Höchbauer, A. Misra, R. G. Hoagland, Nanostructured Cu/Nb multilayers subjected to helium ion-irradiation, *Nucl. Instrum. Methods Phys. Res. Sect. B* 261 (2007) 1129–1132.
 - [24] A. Kashinath, A. Misra, M.J. Demkowicz, Stable storage of helium in nanoscale platelets at semicoherent interfaces, *Phys. Rev. Lett.* 110 (2013), 086101.
 - [25] H.H. Chen, Y.F. Zhao, J.Y. Zhang, Y.Q. Wang, He-ion irradiation effects on the microstructure stability and size-dependent mechanical behavior of high entropy alloy/Cu nanotwinned nanolaminates, *Int. J. Plasticity* 133 (2020), 102839.
 - [26] T. Hochbauer, A. Misra, K. Hattar, R.G. Hoagland, Influence of interfaces on the storage of ion-implanted he in multilayered metallic composites, *J. Appl. Phys.* 98 (2005), 123516.
 - [27] W.J. Weber, Y.W. Zhang, Predicting damage production in monoatomic and multielemental targets using stopping and range of ions in matter code: challenges and recommendations on the use of SRIM for computing radiation damage exposure, *Solid State Mater. Sci.* 23 (2019), 100757.
 - [28] N.A.P. Kiran Kumar, C. Li, K.J. Leonard, H. Bei, S.J. Zinkle, Micro-structural stability and mechanical behavior of FeNiMnCr high entropy alloy under ion irradiation, *Acta Mater.* 113 (2016) 230–244.
 - [29] E. Astm, Standard practice for neutron radiation damage simulation by charged-particle, *Annu. B. ASTM Stand.* 12 (02) (2009) 1–21.
 - [30] L. Dong, H.X. Zhang, H. Amekura, F. Ren, A. Chettah, M.Q. Hong, W.J. Qin, J. Tang, L.L. Hu, H. Wang, C.Z. Jiang, Period-thickness dependent responses of Cu/W multilayered nanofilms to ions irradiation under different ion energies, *J. Nucl. Mater.* 497 (2017) 117–127.
 - [31] Y. Gao, T.F. Yang, J.M. Xue, S. Yan, S.Q. Zhou, Y.G. Wang, D.T.K. Kwok, P.K. Chu, Y.W. Zhang, Radiation tolerance of Cu/W multilayered nanocomposites, *J. Nucl. Mater.* 413 (2011) 11–15.
 - [32] P.B. Zhang, J.J. Zhao, Y. Qin, B. Wen, Stability and dissolution of helium-vacancy complexes in vanadium solid, *J. Nucl. Mater.* 419 (2011) 1–8.
 - [33] K.Y. Tsai, M.H. Tsai, J.W. Yeh, Sluggish diffusion in co-cr-fe-mn-ni high entropy alloys, *Acta Mater.* 61 (2013) 4887–4897.
 - [34] F.F. Zhang, X. Wang, J.B. Wierschke, L.M. Wang, Helium bubble evolution in ion irradiated Al/B4C metal matrix composite, *Scr. Mater.* 109 (2015) 28–33.
 - [35] W.R. Tyson, W.A. Miller, Surface free energies of solid metals: estimation from liquid surface tension measurements, *Surf. Sci.* 62 (1977) 267–276.
 - [36] Z.F. Yan, S.S. Liu, S.Q. Xia, Y. Zhang, Y.G. Wang, T.F. Yang, He behavior in Ni and Ni-based equiatomic solid solution alloy, *J. Nucl. Mater.* 505 (2018) 200–206.
 - [37] Z. Fan, S. Zhao, K. Jin, D. Chen, Y.N. Osetskii, Y. Wang, H. Bei, K.L. More, Y. Zhang, Helium irradiated cavity formation and defect energetics in Ni-based binary single phase concentrated solid solution alloys, *Acta Mater.* 164 (2019) 283–292.
 - [38] D. Chen, Y. Tong, H. Li, J. Wang, Y.L. Zhao, A. Hu, J.J. Kai, Helium accumulation and bubble formation in FeCoNiCr alloy under high fluence He+ implantation, *J. Nucl. Mater.* 501 (2018) 208–216.
 - [39] L.X. Yang, H.L. Ge, J. Zhang, T. Xiong, High he-ion irradiation resistance of CrMnFeCoNi high-entropy alloy revealed by comparison study with Ni and 304SS, *J. Mater. Sci. Technol.* 35 (2019) 300–305.
 - [40] I.R. Brearley, D.A. MacInnes, An improved equation of state for inert gases at high pressures, *J. Nucl. Mater.* 95 (1980) 239–252.
 - [41] A. Loganathan, A.S. Gandhi, Effect of phase transformations on the fracture toughness of t' yttria stabilized zirconia, *Mater. Sci. Eng. A* 556 (2012) 927–935.
 - [42] C.M. Barr, J.E. Nathaniel II, K.A. Unocic, J.P. Liu, Y. Zhang, Y. Wang, M.L. Taheri, Exploring radiation induced segregation mechanism at grain boundaries in equiatomic CoCrFeNiMn high entropy alloy under heavy ion irradiation, *Scr. Mater.* 156 (2018) 80–84.
 - [43] M.R. He, S. Wang, S. Shi, K. Jin, H. Bei, K. Yasuda, S. Matsumura, K. Higashida, I. M. Robertson, Mechanisms of radiation-induced segregation in CrFeCoNi-based single-phase concentrated solid solution alloys, *Acta Mater.* 126 (2017) 182–193.
 - [44] C.L. Xu, X.B. Liu, F. Xue, Y.F. Li, W. Jia, Irradiation-induced BCC-phase formation and magnetism in a 316 austenitic stainless steel, *Nucl. Eng. Tech.* 52 (2020) 610–613.
 - [45] C.L. Xu, X.B. Liu, F. Xue, Y.F. Li, Characterization of magnetic properties in a 316 stainless steel after deformation and irradiation, *Fusion Eng. Des.* 133 (2018) 125–129.
 - [46] A. Kashinath, P. Wang, J. Majewski, J.K. Baldwin, Y.Q. Wang, M.J. Demkowicz, Detection of helium bubble formation at fcc-bcc interfaces using neutron reflectometry, *J. Appl. Phys.* 114 (2013), 043505.
 - [47] A. Kashinath, M.J. Demkowicz, A predictive interatomic potential for He in Cu and Nb, *Model. Simul. Mater. Sci. Eng.* 19 (2011), 035007.
 - [48] N.A.P. Kiran Kumar, C. Li, K.J. Leonard, H. Bei, S.J. Zinkle, Micro-structural stability and mechanical behavior of FeNiMnCr high entropy alloy under ion irradiation, *Acta Mater.* 113 (2016) 230–244.
 - [49] M.J. Demkowicz, D. Bhattacharyya, I. Usov, Y.Q. Wang, M. Nastasi, A. Misra, The effect of excess atomic volume on He bubble formation at fcc-bcc interfaces, *Appl. Phys. Lett.* 97 (2010) 846.
 - [50] T.D. Shen, Radiation tolerance in a nanostructure: is smaller better? *Nucl. Instrum. Methods Phys. Res. Sect. B* 266 (2008) 921–925.
 - [51] G. Gottstein, L.S. Shvindlerman, Grain Boundary Migration in Metals Thermodynamics Kinetics Applications, CRC Press, Boca Raton, Florida, 1999.
 - [52] T.D. Shen, C.C. Koch, T.L. McCormick, R.J. Nemanich, J.Y. Huang, The structure and property characteristics of amorphous/nanocrystalline silicon produced by ball milling, *J. Mater. Res.* 10 (1995) 139–148.
 - [53] M. Rose, A.G. Balogh, H. Hahn, Instability of irradiation induced defects in nanostructured material, *Nucl. Instrum. Methods Phys. Res. Sect. B* 127–128 (1997) 119–122.
 - [54] Y. Zhang, G.M. Stocks, K. Jin, C.Y. Lu, H.B. Bei, B.C. Sales, L.M. Wang, R.E. Stoller, G.D. Samolyuk, M. Caro, A. Caro, W.J. Weber, L.K. Beland, Influence of chemical disorder on energy dissipation and defect evolution in concentrated solid solution alloys, *Nat. Commun.* 6 (2015) 8736.
 - [55] A.D. Marwick, Segregation in irradiated alloys: inverse kirkendall effect and effect of constitution on void swelling, *J. Phys. F-Metal Phys.* 8 (1978) 1849–1861.
 - [56] J.A. Brinkman, On the nature of radiation damage in metals, *J. Appl. Phys.* 25 (1954) 961.
 - [57] T. Nagase, P.D. Rack, J.H. Noh, T. Egami, In-situ TEM observation of structural changes in nano-crystalline CoCrCuFeNi multicomponent high-entropy alloy (HEA) under fast electron irradiation by high voltage electron microscopy (HVEM), *Intermetallics* 59 (2015) 32–42.
 - [58] G.S. Was, Fundamentals of radiation materials science, *Mater. Today* 10 (2007).
 - [59] M. Vaidya, K.G. Pradeep, B.S. Murty, G. Wilde, S.V. Divinski, Bulk tracer diffusion in CoCrFeNi and CoCrFeMnNi high entropy alloys, *Acta Mater.* 146 (2018) 211–224.
 - [60] M. Vaidya, S. Trubel, B.S. Murty, G. Wilde, S.V. Divinski, Ni tracer diffusion in CoCrFeNi and CoCrFeMnNi high entropy alloys, *J. Alloys Compd.* 688 (2016) 994–1001.
 - [61] J. Dabrowa, W. Kucza, Interdiffusion in the FCC-structured Al-Co-Cr-Fe-Ni high entropy alloys: experimental studies and numerical simulations, *J. Alloys Compd.* 674 (2016) 455–462.
 - [62] S. Sun, et al., Segregation of Al_{1.5}CrFeNi high entropy alloy induced by vacancy-type defects, *Scripta Mater.* 161 (2019) 40–43.
 - [63] W.T. Lin, G.M. Yeli, G. Wang, J.H. Lin, S.J. Zhao, D. Chen, S.F. Liu, F.L. Meng, Y. R. Li, F. He, Y. Lu, J.J. Kai, He-enhanced heterogeneity of radiation-induced segregation in FeNiCoCr high-entropy alloy, *J. Mater. Sci. Technol.* 101 (2022) 226–233.
 - [64] T.F. Yang, et al., Effects of Al addition on microstructure and mechanical properties of AlxCoCrFeNi high-entropy alloy, *Mater. Sci. Eng. A* 648 (2015) 15–22.